Journal of Nuclear Materials 400 (2010) 79–83

Contents lists available at ScienceDirect

Journal of Nuclear Materials

journal homepage: www.elsevier.com/locate/jnucmat

On the black oxide colour of zirconium alloys

Pia Tejland *, Christoph Langhammer, Hans-Olof Andrén

Dept. of Applied Physics, Chalmers University of Technology, SE-412 96 Göteborg, Sweden

ARTICLE INFO

Article history:
Received 13 January 2010
Accepted 14 February 2010

ABSTRACT

Tubes of four zirconium alloys, used as cladding materials in light water nuclear reactors, were oxidized in an autoclave to produce oxide layers 1, 2 and 9 μm thick. The reflectance of the tubes was measured using a UV–vis–NIR spectrophotometer equipped with an integrating sphere detector. The 1 and 2 μm oxide tubes had a black appearance and a reflectance of only 10–12% in the visible region, whereas a dark grey appearing 9 μm oxide tube had 13–17% reflectance. The low reflectance was interpreted in terms of localized surface plasmon resonance in metallic particles embedded in the oxide layer, having a mean size of 40–70 nm.

1. Introduction

It is well known that Zircaloy-type zirconium alloys used as cladding materials in nuclear reactors turn black upon oxidation [1,2]. During further oxidation the oxide slowly turns grey [1,2]. By contrast, the oxide that forms on very pure zirconium is white [1]. Fig. 1 shows an example where samples of a cladding tube of a Zircaloy-2 material have been exposed to oxidation in autoclave (400 or 415 °C at 10.3 MPa). The shiny un-oxidized metal has turned black when the oxide has grown to a thickness of 1 μm and it is still black for a 2 μm thick oxide. After oxidation to an oxide thickness of 9 μm, the appearance is dark grey (Fig. 1).

In this paper, integrating sphere measurements are presented that quantify light absorption by different oxide thickness of the same materials, as well as approximately equally thick oxides on different zirconium alloys. The data obtained are interpreted in terms of localized surface plasmon resonances (LSPRs) in intermetallic particles embedded in the oxide. In a simple picture the LSPR can be rationalized as a resonant collective oscillation of the electrons in the particle that can be described as an electric point dipole. Typically, LSPRs appear in the UV, visible and near-IR regions of the electromagnetic (EM) spectrum and can be directly excited by the EM field of incident light. The resonance frequency of the LSPR depends typically on the nanoparticle size, shape and electronic structure, i.e. its dielectric properties, as well as on the refractive index of the particle environment. LSPR is an inherent feature of, in principle, all metallic nanoparticles whose "strength" (i.e. lifetimes and optical cross-sections) strongly depend on the dielectric properties of the metal at optical frequencies [3–7]. Transition metals like Pt, Pd or Ni, with d-bands extending up to the Fermi level, typically exhibit relatively broad LSPR bands dominated by optical absorption [3–5]. Similar LSPR-properties are expected for the intermetallic particles embedded in the oxide in this study.

2. Experimental

The composition of the four studied materials is given in Table 1. Three are variants of the common cladding material Zircaloy-2, and the fourth is a Sn–Nb–Fe containing zirconium alloy also used commercially as a cladding material in light water reactors. All four materials exhibit a black oxide. These zirconium alloys all contain small precipitates, usually designated second phase particles (SPP). In Zircaloy-2 materials (Materials A, B and C) they are of the intermetallic $Zr(Fe,Cr)_2$ and $Zr_2(Fe,Ni)$ types [8], and in the Zr–Sn–Nb–Fe material (Material D) they are of β-Nb type and a Zr–Nb–Fe phase [9]. The size distribution of SPPs was measured on micrographs recorded using a field emission gun scanning electron microscope (FEG–SEM) at 30,000× magnification; one example of a micrograph of Material B is given in Fig. 2.

Oxidation of 5 cm long tube samples was performed in steam (water conductivity less than 1 μS cm^{-1}) in a static autoclave using a pressure of 10.3 MPa and a temperature of 400 °C (for the two thinner oxides) or 415 °C (for the thickest oxide) for times up to 60 days. The time of oxidation was chosen to give approximately 1, 2 and 9 μm of oxide; the measured weight gains are given in Table 2 (15 mg/dm^2 corresponds to approximately 1 μm of oxide).

Thin foil cross-sections of the metal/oxide interface were characterized using transmission electron microscopy (TEM) techniques. Details of specimen preparation and microscopy procedures used are found elsewhere [10].

* Corresponding author. Tel.: +46 31 772 3137; fax: +46 31 772 3224.
E-mail address: pia.tejland@chalmers.se (P. Tejland).

0022-3115/$ - see front matter © 2010 Elsevier B.V. All rights reserved.
doi:10.1016/j.jnucmat.2010.02.013

Fig. 1. Five centimeter long tube specimens of Zircaloy-2 (from left to right:) unoxidized; with 1 μm thick oxide; with 2 μm thick oxide; and with 9 μm thick oxide. (For interpretation of the references to colour in this figure legend, the reader is referred to the web version of this article.)

Table 1
Composition of the four materials studied.

Material designation	Type	Composition (wt.%)				
		Sn	Fe	Cr	Ni	Nb
A	Zircaloy-2	1.46	0.12	0.10	0.05	–
B	Zircaloy-2	1.32	0.17	0.10	0.05	–
C	Zircaloy-2	1.32	0.17	0.10	0.05	–
D	Zr–Sn–Nb–Fe	0.92	0.10	–	–	0.9

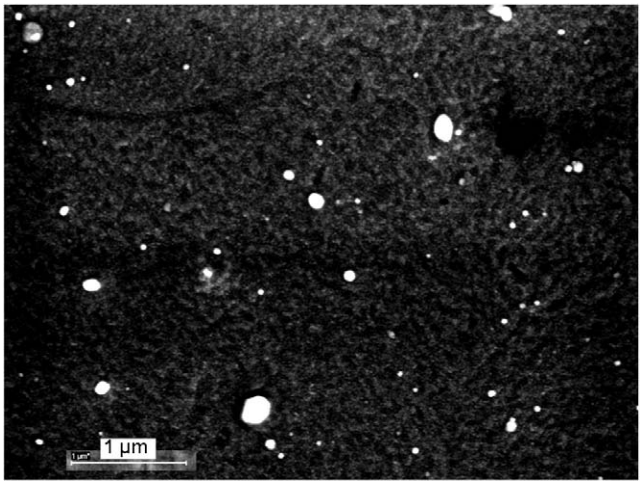

Fig. 2. SEM micrograph of Material B, showing SPPs (bright).

Table 2
Weight gains after oxidation in steam autoclave using the time and temperature given. Oxide thickness is calculated using the relation 15 mg/dm^2 equals 1 μm.

Material	Temperature (°C)	Time (days)	Weight gain (mg/dm^2)	Oxide thickness (μm)
A	400	6	33.9	2.26
B	400	3	17.8	1.19
B	400	15	29.2	1.95
B	415	60	133.6	8.91
C	400	15	27.5	1.83
D	400	15	28.5	1.90

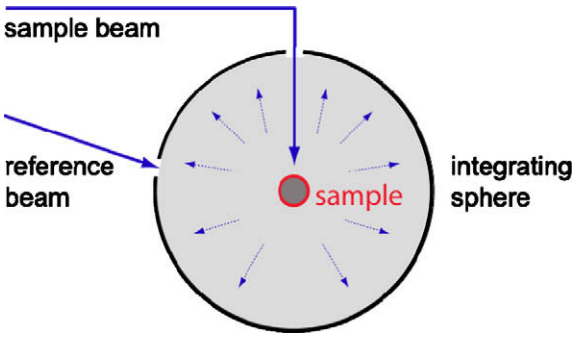

Fig. 3. Integrating sphere set-up. (For interpretation of the references to colour in this figure legend, the reader is referred to the web version of this article.)

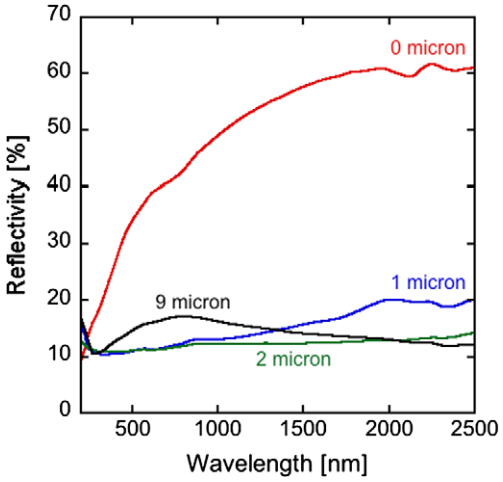

Fig. 4. Reflectance of tube samples of Material B with different oxide thickness. (For interpretation of the references to colour in this figure legend, the reader is referred to the web version of this article.)

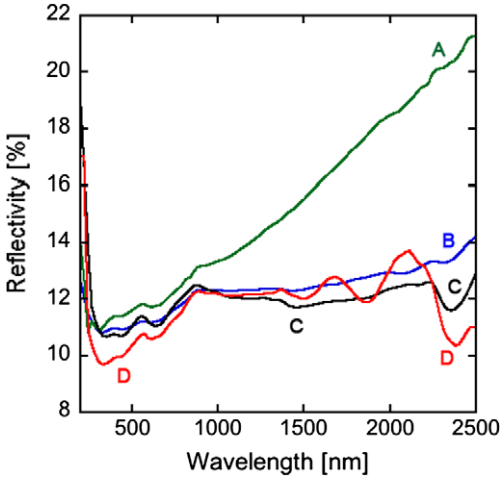

Fig. 5. Reflectance of tube samples of different materials, all with approximately 2 μm oxide thickness. (For interpretation of the references to colour in this figure legend, the reader is referred to the web version of this article.)

The light reflection of the cylindrical samples was measured in an ultraviolet–visual–near infrared (UV–vis–NIR) spectrophotometer (Varian Cary 5000), using a small spot kit to focus the probing light beam (beam diameter ≈ 3 mm) and an integrating sphere

detector (internal DRA 2500). During the integrating sphere experiments (see Fig. 3 for a schematic drawing), the samples were mounted in the center of the integrating sphere detector. Comparing the total scattering signal collected by the integrating sphere for the samples with a reference (Labsphere Spectralon), which exerts more than 99% reflectance in the spectral range between 350 and 1800 nm and more than 96% reflectance in the range between 200 and 2500 nm (6–0.5 eV) yielded the sample reflection coefficient [6].

3. Results

The light reflection of Material B, un-oxidized and with 1, 2 and 9 μm oxide, is shown in Fig. 4. The reflectance of the un-oxidized sample is between 29% and 44% in the visible region (400–800 nm). These relatively low reflectance values for a metallic surface (below the bulk plasma frequency) are explained by the cylindrical geometry of the studied samples. Independent of sample orientation with respect to the incoming sample beam, this geometry leads to the specularly reflected light exiting the integrating sphere detector through the entrance port (Fig. 3), without being detected and thus decreasing the measured apparent reflectance. For comparison of samples with identical geometries as in the present work this is, however, not a problem as long as the *absolute* reflectance is not compared to measurements obtained from specimens with different geometry.

Analyzing the reflectance of the oxidized samples yields a low value of 11–12% for the 1 and 2 μm oxide thicknesses. Obviously, such a low (with respect to the un-oxidized samples) and wavelength independent reflectance is in accordance with the black appearance of these samples. The 9 μm oxide sample had a slightly higher reflectance, 13–17%, consistent with its dark greyish appearance. It is interesting to note that for the shortest wavelengths in the ultraviolet region, 250–300 nm, the reflectance is higher. In the near infrared region (800–2500 nm), the reflectance increases for the 1 μm oxide sample, stays rather constant for the 2 μm sample and decreases for the 9 μm oxide sample.

Reflection measurements on four different materials, all oxidized to approximately 2 μm oxide thickness, are shown in Fig. 5. Material C behaves similarly to Material B in the visible region, while Material A has a slightly higher reflectance and Material D the lowest of all studied materials, between 10% and 11% in the visible region. Oxidized Material D also has the blackest visual appearance of the materials, but the difference is not large enough to be illustrated in a photograph. As in the case for the Material B samples, all samples have a higher reflectance further down in UV wavelength. Reflection in the NIR region is rather constant at 12–13% for all materials except Material A, which has an increasing reflectance up to 21% at the longest measured wavelength (2500 nm). There are some reflectance fluctuations with wavelength, in particular in NIR for Material D.

The SPP size distribution determined for Material B is given in Fig. 6, and Table 3 gives particle size data for all four materials. The size distributions all start around 10 nm. The mean size is between 40 and 70 nm, and the largest particles found are between 240 and 440 nm.

Table 3
Particle sizes (μm).

Material	SPP type	Minimum diameter	Mean diameter	Maximum diameter
A	$Zr(Fe,Cr)_2$ and	0.01	0.06	0.24
B	$Zr_2(Fe,Ni)$	0.01	0.04	0.44
C		0.01	0.07	0.25
D	β-Nb and Zr–Nb–Fe	0.01	0.07	0.31

4. Discussion

As shown in Table 3, SPPs in all four studied materials are in the range 10–440 nm. These particles are nobler than the matrix of the zirconium alloys, so when the materials are oxidized, particles are not immediately oxidized but retain their metallic character for a long time [10,11]. Fig. 7 shows a scanning transmission electron microscopy/energy dispersive X-ray spectrometry (STEM/EDX) analysis of an SPP inside the oxide layer of Material A, demonstrating the metallic character of these particles. Thus, at least the thinner oxides (1–2 μm) contain small metallic particles, embedded in a dielectric medium, zirconia.

As described above, such systems of metal nanoparticles embedded in a dielectric material may exhibit LSPR, causing them to absorb light at UV–vis–NIR wavelengths, the maximum absorption wavelength being determined by particle size and shape and

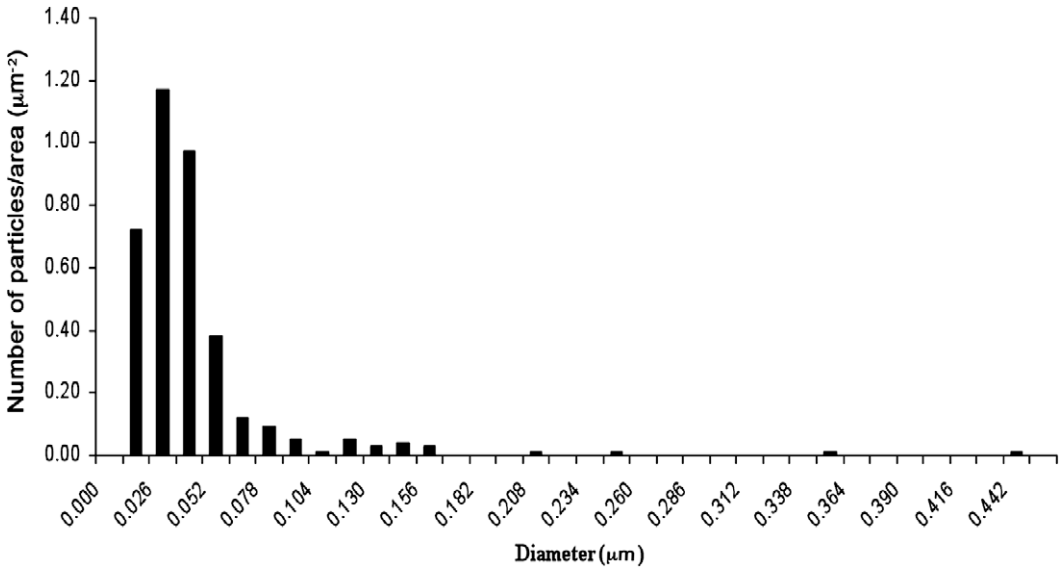

Fig. 6. Particle size distribution for Material C, as determined by FEG-SEM.

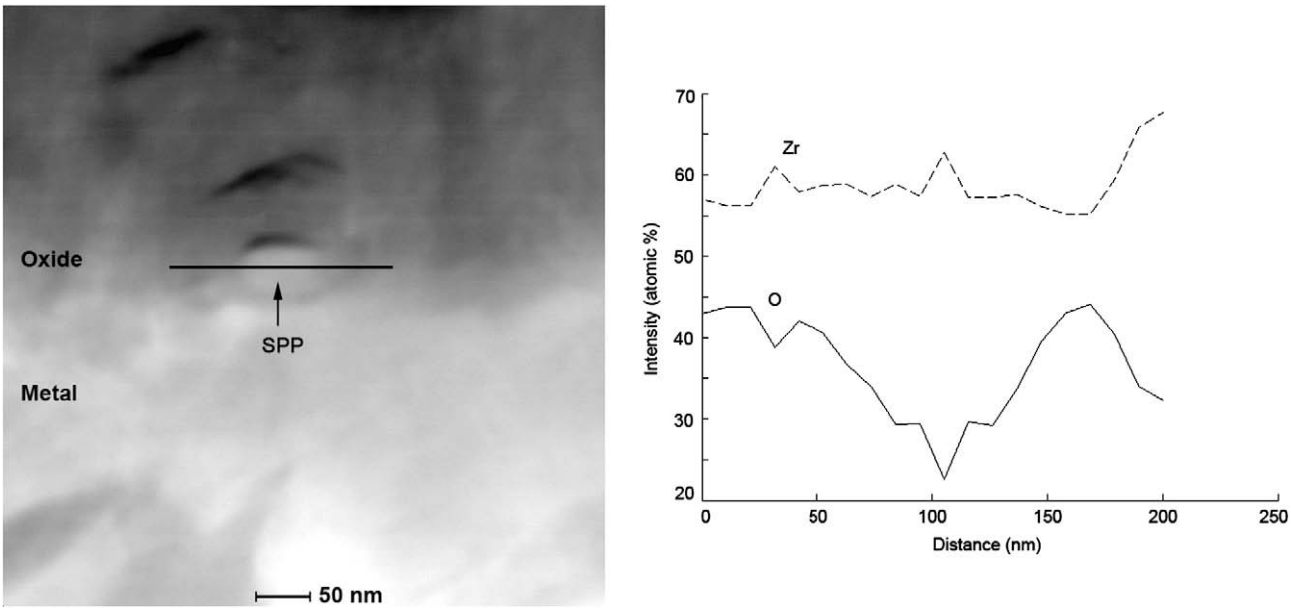

Fig. 7. Scanning transmission electron microscopy (STEM) micrograph of an SPP embedded in the oxide of Material C (left); energy dispersive X-ray spectrometry (EDX) linescan across the particle demonstrating that it is not oxidized (right).

the dielectric properties of both the particle and the surrounding materials [3–5,12,13].

For particles much smaller than the wavelength of light (i.e. in the so-called quasistatic regime), the LSPR frequency ω_{LSPR} can be approximated by [7]:

$$\omega_{LSPR} = \omega_P/\sqrt{(1+2\varepsilon_D)}$$

where ω_P is the bulk plasmon frequency of the metal (in radians/s) and ε_D the dielectric constant of the embedding medium, in our case zirconia. This frequency is independent of particle size. However, if the particles have a diameter comparable to the wavelength of light, additional phenomena (retardation or finite wavelength effects such as dynamic depolarization and radiation damping [13–15]) occur. These effects may be accounted for by the so-called modified long wavelength approximation that describes the optical properties of nanoparticles in the range 10–200 nm quite accurately [4,6].

To apply the theory to the oxide on zirconium alloys, numerical values for the dielectric constant of zirconia and the bulk plasmon energies of the various SPPs are needed. The dielectric constant at energies corresponding to visible light (1.5–3 eV) for monoclinic ZrO_2 (the dominating structure of zirconia that forms on zirconium alloys in autoclave testing) can be estimated from the refractive index in the visible and infrared, which was determined by Wilkins [16] to $n = 2.0$. Since the integrated loss function of monoclinic ZrO_2 is very small below 4 eV [17], we can estimate the dielectric constant using Maxwell's relation $\varepsilon_D = n^2$ to 4.0.

In addition, the bulk plasmon energies of the intermetallic compounds involved and, for Material D, of β-Nb are needed. To our knowledge, the bulk plasmon energies of the intermetallic compounds have not yet been measured. Inspection of energy-loss spectra of the pure elements involved (Zr, Fe, Cr, Ni, Nb) generally show two peaks: one (usually larger) at around 25 eV, and one smaller at 6–16 eV with Zr and Nb at the higher end of this interval [18]. Both peaks represent bulk plasmon resonances in the material, the higher energy peak due to the collective motion of all valence electrons and the smaller involving only groups of electrons, as demonstrated by Romaniello et al. [19] for metals belonging to group-VB and VIB in the periodic system. In the absence of any data we assume that the plasmon energies in the various intermetallic compounds are in the same range as their constituent pure elements. For our further analysis it is not *a priori* clear which one of the two bulk plasmon frequencies (i.e. high or low energy) that should be used. If we focus on the second, lower energy plasmon peak around 13 eV (the dominating SPP in Material D is β-Nb, and Nb has a plasmon energy at 13.0 eV [19]) this would correspond to an LSPR energy of 4.33 eV or a wavelength of 286 nm. At this UV wavelength we may therefore expect to have the absorption maximum if the particles are very small compared to the wavelength of light. For the high-energy plasmon peak around 25 eV, we arrive at a LSPR of 8.3 eV. This corresponds to a wavelength of only 149 nm, far away from the visible part of the spectrum.

For spherical particles with sizes comparable to the wavelength of light (i.e. 400–800 nm), the effects of radiation damping and dynamic depolarization will cause a red-shift of LSPR peak. The approximate expression for the polarizability of a sphere is:

$$\alpha(\omega) = 4\pi(D/2)^3\omega_{LSPR}^2/(\omega_{LSPR}^2 - \omega^2 - i\Gamma\omega)$$

where D is the particle diameter and Γ the damping constant (quantifying, e.g. damping via interband excitations).

In the modified long-wave approximation this expression is modified to [13]:

$$\alpha'(\omega) = \alpha(\omega)\left[1 - i(k^3/6\pi)\alpha(\omega) - (k^2/2\pi D)\alpha(\omega)\right]^{-1}$$

where k is the wavevector of the light ($k = 2\pi/\lambda = \omega/c$).

Inserting the expression for $\alpha(\omega)$, we find that $\alpha'(\omega)$ will have a resonance ω_R when

$$(2\omega_{LSPR}^2 - 2\omega^2)/\pi D^3\omega_{LSPR}^2 - k^2/(2\pi D) = 0$$

$$\text{or } \omega_R = \omega_{LSPR}/\sqrt{\left(1 + \omega_{LSPR}^2 D^2/4c^2\right)}$$

For $D = 10$ nm, the read-shift is small as expected (288 nm instead of 286 nm) but it increases with particle size to 312, 342, 360, 835 and 1411 nm for $D = 40$, 60, 70, 250 and 440 nm, respectively. We therefore expect to obtain absorption starting at 290 nm, peaking at 310–360 nm and remaining at least up to

800 nm. Taking further into account the effect of the not perfectly spherical SPP-geometries introduces additional significant spectral red-shifts of the LSPRs in the system [13]. These results compare very well with the measured reflectance curves in Fig. 5. After a fast decrease in reflectance at around 300 nm, the minimum reflectance is found around 350 nm followed by an increase up to 800 nm. The fact that the reflectance stays at a low level from 800 nm up to at least 2500 nm in Materials B, C and D suggests that the size distributions in these materials have a tail of larger particles not captured by the counting of some 200 particles. Only in Material B a particle as large as 440 nm in diameter was encountered. The fast increase in reflectance for Material A suggests that there is a shorter tail of the size distribution in this material. However this could not be measured with the limited number of particles studied.

The fluctuation in reflectance for wavelengths larger than 1500 nm is most probably an interference effect. Wilkins [16] studied the reflectance of oxide films on pure zirconium using a vis-IR spectrophotometer at wavelengths up to 15 μm. Using his graphs, the reflection minima observed for Material D at 1500, 1800 and 2400 nm fit with the 6th, 5th and 4th order reflectance minima for an oxide thickness of 2.2 μm, in good agreement with the oxide thickness of 1.90 μm calculated from the weight gain. The slightly too large thickness determined may be due to a slightly larger effective light path in our experiments, due to the curved surfaces of the cylindrical samples. Also Material C (1.83 μm thick oxide) exhibits the 2400 nm reflectance minimum, whereas Materials A and B do not show any interference effects.

Fig. 4 shows the development of reflectance with oxide thickness. There is no large difference between the 1 μm and 2 μm oxide layers, suggesting that the light sees un-oxidized particles in both oxides. However, in the 9 μm oxide, the reflectance is higher, in particular in the wavelength region around 800 nm, corresponding to the larger particles (250 nm). This suggests that the particles are under oxidation so that only a smaller metallic core is embedded in this oxide, shifting the LSPR of the remaining metallic core towards shorter wavelength. Also, light has to travel further into the oxide before it meets un-oxidized particles. Although zirconia is transparent, oxide layers thicker than a few microns contain lateral cracks, parallel to the metal–oxide interface and up to 1 μm wide [10], further increasing the reflectance and giving the oxide a greyish appearance.

5. Conclusions

The reason for the black appearance of oxidized Zr–Fe–Cr–Ni and Zr–Nb alloys is the excitation of localized surface plasmon resonances in metallic particles embedded in the oxide layer.

Particle size distributions peaking around 40–70 nm and extending to at least 250 nm give a low reflectance in the visible and NIR region.

Acknowledgements

The SPP size distributions were measured by Sorina Ciurea at Sandvik Materials Technology. Financial support was received from Sandvik AB, Westinghouse Electric Sweden AB, Vattenfall Bränsle AB, OKG AB and the Swedish Radiation Protection Agency. One of us (C.L.) also acknowledges financial support from the "Multifunctional photoactive nanoparticles, nanoparticle arrays and nanoarchitectures" (PhotoNano) program of the Swedish Foundation for Strategic Research (SSF).

References

[1] B. Cox, Advances in Corrosion Science and Technology 5 (1975) 173–391.
[2] E. Hillner, Corrosion of zirconium-base alloys—an overview, in: A.L. Lowe, Jr., G.W. Parry, (Eds.), Zirconium in the Nuclear Industry, ASTM STP 633, American Society for Testing and Materials, 1977, pp. 211–235.
[3] T. Pakizeh, C. Langhammer, I. Zoric, P. Apell, M. Käll, Nano Letters 9 (2009) 882–886.
[4] C. Langhammer, Z. Yuan, I. Zoric, B. Kasemo, Nano Letters 6 (2006) 833–838.
[5] C. Langhammer, B. Kasemo, I. Zoric, Journal of Chemical Physics 126 (2007) 194702-1–194702-11.
[6] C. Langhammer, M. Schwind, B. Kasemo, I. Zoric, Nano Letters 8 (2008) 1461–1471.
[7] C.F. Bohren, D.R. Huffman, Absorption and Scattering of Light by Small Particles, Wiley-Interscience, New York, 1983.
[8] C. Lemaignan, A.T. Motta, Zirconium alloys in nuclear applications, in: R.W. Cahn, P. Haasen, E.J. Kramer (Eds.), Materials Science and Technology, vol. 10B (Chapter 7).
[9] R.J. Comstock, G. Schoenberger, G. Sabol, Influence of processing variables and alloy chemistry on the corrosion behavior of ZIRLO nuclear fuel cladding, in: E.R. Bradley, G.P. Sabol (Eds.), Zirconium in the Nuclear Industry: Eleventh International Symposium, ASTM STP 1295, ASTM International, West Conshohocken, PA, 1996, pp. 710–723.
[10] P. Tejland, M. Thuvander, H.-O. Andrén, S. Ciurea, T. Andersson, M. Dahlbäck, L. Hallstadius, Detailed microstructure of the metal/oxide interface region in Zircaloy-2 after autoclave corrosion testing, Proceedings of Zirconium in the Nuclear Industry: 16th International Symposium, Chengdu, China, May 9–13, 2010, submitted for publication.
[11] D. Pêcheur, F. Lefebvre, A.T. Motta, C. Lemaignan, D. Carquet, Oxidation of intermetallic precipitates in Zircaloy-4: impact of irradiation, in: A.M. Garde, E.R. Bradley (Eds.), Zirconium in the Nuclear Industry: Tenth International Symposium, ASTM STP 1245, American Society for Testing and Materials, Philadelphia, 1994, pp. 687–708.
[12] T.R. Jensen, M.L. Duval, K.L. Kelly, A.A. Lazarides, G.C. Schatz, R.P. Van Duyne, Journal of Physical Chemistry B 103 (1999) 9846–9853.
[13] K.L. Kelly, E. Coronado, L.L. Zhao, G.C. Schatz, Journal of Physical Chemistry B 107 (2003) 668–677.
[14] A. Wokaun, J.P. Gordon, P.F. Liao, Physical Review Letters 48 (1982) 957–960.
[15] M. Meier, A. Wokaun, Optics Letters 8 (1983) 581–583.
[16] N.J.M. Wilkins, Corrosion Science 4 (1964) 17–24.
[17] L.K. Dash, N. Vast, P. Baranek, M.-C. Cheynet, L. Reining, Physical Review B 70 (2004) 245116-1–245116-17.
[18] C.C. Ahn, O.L. Krivanek, EELS Atlas, Gatan Inc., Warrendale PA, USA, 1983.
[19] P. Romaniello, P.L. de Boeij, F. Carbone, D. van der Marel, Physical Review B 73 (2006) 075115-1–075115-16.